Journal of Computational Physics **171,** 336–356 (2001)
doi:10.1006/jcph.2001.6791, available online at http://www.idealibrary.com on IDEAL®

A Characteristic Galerkin Method for Discrete Boltzmann Equation

Taehun Lee and Ching-Long Lin

Department of Mechanical Engineering and Iowa Institute of Hydraulic Research, The University of Iowa, Iowa City, Iowa 52242
E-mail: ching-long-lin@uiowa.edu

Received September 18, 2000; revised March 26, 2001

The characteristic Galerkin finite element method for the discrete Boltzmann equation is presented to simulate fluid flows in complex geometries. The inherent geometric flexibility of the finite element method permits the easy use of simple Cartesian variables on unstructured meshes and the mesh clustering near large gradients. The characteristic Galerkin procedure with appropriate boundary condition results in accurate solutions with little numerical diffusion. Several test cases are conducted, including unsteady Couette flows, lid-driven cavity flows, and steady flow past a circular cylinder on unstructured meshes. The numerical results are in good agreement with previous analytical (if applicable), numerical, and experimental results. © 2001 Academic Press

Key Words: lattice Boltzmann equation; characteristic Galerkin method; unstructured mesh.

1. INTRODUCTION

The lattice Boltzmann equation (LBE) method has been demonstrated to be an effective tool in simulating flow through porous media, multiphase flow, and interfacial flow phenomena [1]. The conventional LBE method, however, requires regular structured meshes. Since He and Luo [2, 3] and Abe [4] demonstrated that the LBE is a discretized form of the continuous Boltzmann equation and the discretization of physical space is not coupled with the discretization of momentum space, several efforts have been made to address the issue concerning the treatment of curved boundaries and the control of grid density at desirable regions. Significant progress has been achieved in recent years.

Filippova and Hänel [5] developed a second-order accurate boundary condition for the LBE method to treat a curved boundary on the regular structured mesh. Mei *et al.* [6] improved this scheme and further extended it to three dimensions [7]. He *et al.* [8–10] proposed an interpolation-supplemented LBE model (ISLBE) to simulate a two-dimensional channel flow with sudden expansion on a nonuniform mesh, and steady and unsteady flows past a

0021-9991/01 $35.00
Copyright © 2001 by Academic Press
All rights of reproduction in any form reserved.

circular cylinder in a curvilinear coordinate system. This method adds a new interpolation step between the streaming and relaxation steps in the conventional LBE method and retains the locality property of the two steps. Cao *et al.* [11] indicated that the LBE method is a special finite-difference discretization of the kinetic equation of the discrete velocity distribution function, and thus the application of nonuniform meshes and semiimplicit collision scheme to the LBE is possible. On this basis, Mei and Shyy [12] developed a LBE method in a generalized body-fitted coordinate system, solving fluid flow problems in complex geometries. Succi *et al.* [13] and Xi *et al.* [14, 15] proposed finite-volume LBE methods for simulation of fluid flows in complex geometries.

In order to solve the LBE in complex geometries while preserving the advantages of the conventional LBE method such as data locality and little numerical diffusion, we present the characteristic Galerkin finite element method [16] for solving the discrete Boltzmann equation (CGDBE). For scalar variables with constant source terms, the characteristic Galerkin method, which utilizes the optimal approximation along the characteristics, is identical to the Taylor–Galerkin method [17, 18]. The Taylor–Galerkin method is a generalization of the Lax–Wendroff method [19] in the context of finite elements.

Since the inherent geometric flexibility of the finite element method permits the easy use of simple Cartesian variables on unstructured mesh for arbitrary complex geometries [20], there is no need for global mapping and global transformation of equations to covariant (or contravariant) components. Since the spatial domain is discretized at the element level and interelemental communications are required only when the discretized matrix is solved by the conjugate-gradient type iterative solver, the finite element method can exploit the parallelism in a straightforward manner. In addition, this matrix is well-conditioned and the conjugate-gradient algorithm is favorable to parallelism.

If the original differential operator is self-adjoint (symmetric), the Galerkin spatial discretization of the operator is also self-adjoint. This feature makes the Galerkin discretization of the discrete Boltzmann equation along the characteristics optimal and helps to reduce numerical error. It is noteworthy that Matsushita [21] applied the standard Galerkin method to the one-dimensional continuous Boltzmann equation, but did not utilize the feature of self-adjointness.

This paper is organized as follows. In Section 2, the numerical formulation of the CGDBE, the boundary condition, and the accuracy and stability analyses are described. The present CGDBE method is applied to solve three test cases: unsteady Couette flows, lid-driven cavity flows, and steady flows past a circular cylinder. The numerical results are presented in Section 3 and are compared with previous numerical results. Concluding remarks are given in Section 4.

2. NUMERICAL FORMULATIONS

In this section we present the governing equations, the numerical formulations of the CGDBE, the boundary condition, and the accuracy and stability analyses.

2.1. *Governing Equation*

The continuous Boltzmann equation with the Bhatnagar–Gross–Krook collision operator [22] reads

$$\frac{\partial f}{\partial t} + \boldsymbol{\xi} \cdot \boldsymbol{\nabla} f = -\frac{1}{\lambda}\left(f - f^{(0)}\right), \tag{1}$$

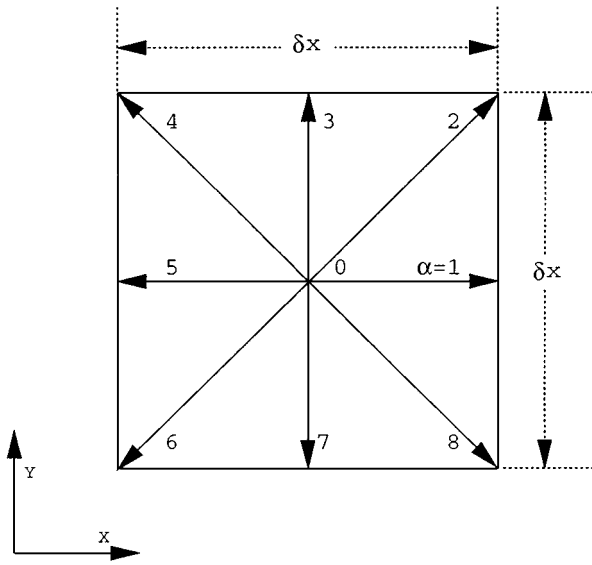

FIG. 1. Two-dimensional square lattice model with a length scale δx.

where f is the single-particle distribution function, $\boldsymbol{\xi}$ is the microscopic velocity, ∇f is the gradient of the function f, λ is the relaxation time due to collision, and $f^{(0)}$ is the Maxwell–Boltzmann distribution function. If a nine-velocity LBE model on a square lattice is used, and the Boltzmann–Maxwellian distribution $f^{(0)}$ is expanded as a Taylor series up to $(\mathbf{u}\cdot\mathbf{u})$, we obtain the discrete Boltzmann equation [23]

$$\frac{\partial f_\alpha}{\partial t} + \mathbf{e}_\alpha \cdot \nabla f_\alpha = -\frac{1}{\lambda}\left(f_\alpha - f_\alpha^{eq}\right), \tag{2}$$

where $\alpha = 0, 1, \ldots, 8$. The discrete velocity $\mathbf{e}_\alpha$ is expressed as (refer to Fig. 1 for the direction represented by the subscript α)

$$\mathbf{e}_\alpha = \begin{cases} (0,0) & \alpha = 0 \\ (\cos\theta_\alpha, \sin\theta_\alpha), & \theta_\alpha = (\alpha-1)\pi/4, \quad \alpha = 1,3,5,7 \\ \sqrt{2}(\cos\theta_\alpha, \sin\theta_\alpha), & \theta_\alpha = (\alpha-1)\pi/4, \quad \alpha = 2,4,6,8. \end{cases} \tag{3}$$

The equilibrium distribution function f_α^{eq} is defined as

$$f_\alpha^{eq} = w_\alpha \rho \left[1 + 3(\mathbf{e}_\alpha \cdot \mathbf{u}) + \frac{9}{2}(\mathbf{e}_\alpha \cdot \mathbf{u})^2 - \frac{3}{2}(\mathbf{u}\cdot\mathbf{u})\right], \tag{4}$$

with the weights $w_0 = 4/9$, $w_1 = w_3 = w_5 = w_7 = 1/9$, and $w_2 = w_4 = w_6 = w_8 = 1/36$ [2]. The macroscopic density ρ and velocity vector $\mathbf{u}$ are related to the distribution function by

$$\sum_{\alpha=0}^{8} f_\alpha = \rho, \quad \sum_{\alpha=1}^{8} \mathbf{e}_\alpha f_\alpha = \rho\mathbf{u}. \tag{5}$$

The pressure can be calculated from $p = c_s^2\rho$ with the speed of sound $c_s = 1/\sqrt{3}$ and the viscosity of the fluid is $\nu = \lambda c_s^2$.

2.2. *Characteristic Galerkin Approximation*

In what follows, the characteristic Galerkin procedure by Zienkiewicz and Codina [16] will be applied to the discrete Boltzmann equation Eq. (2). Let $\tilde{\mathbf{x}}(\mathbf{x}_{ref}, t_{ref}; t)$ denote the trajectory (or characteristic) of the particle that passes the spatial point $\mathbf{x}_{ref}$ at time $t = t_{ref}$, so that $\tilde{\mathbf{x}}(\mathbf{x}_{ref}, t_{ref}; t_{ref}) = \mathbf{x}_{ref}$. Here $\mathbf{x}_{ref}$ is an arbitrary point on the trajectory of the particle between time t_n and t_{n+1}. Thus, the left-hand side of Eq. (2) can be expressed as

$$\frac{d}{dt} f_\alpha(\tilde{\mathbf{x}}(t), t)\bigg|_{t=t_{ref}} = \left(\frac{\partial f_\alpha}{\partial t} + \mathbf{e}_\alpha \cdot \boldsymbol{\nabla} f_\alpha\right)\bigg|_{\mathbf{x}=\mathbf{x}_{ref}, t=t_{ref}}, \tag{6}$$

where $\mathbf{x}_{ref}$ and t_{ref} in $\tilde{\mathbf{x}}(\mathbf{x}_{ref}, t_{ref}; t)$ are omitted for brevity. It is understood that the convective term disappears along the characteristics. Since $\tilde{\mathbf{x}} = \mathbf{x}_{ref}$ at $t = t_{ref}$, Eq. (2) may be recast as

$$\frac{d}{dt} f_\alpha(\tilde{\mathbf{x}}(t), t) = -\frac{1}{\lambda}\big[f_\alpha(\tilde{\mathbf{x}}(t), t) - f_\alpha^{eq}(\tilde{\mathbf{x}}(t), t)\big], \tag{7}$$

which becomes self-adjoint in space and the standard Galerkin spatial approximation of the equation is optimal.

Assume that f_α at time t_n is known and we want to compute it at time t_{n+1}. The discretization of Eq. (7) in time yields

$$\begin{aligned} f_\alpha(\tilde{\mathbf{x}}(t_{n+1}), t_{n+1}) - f_\alpha(\tilde{\mathbf{x}}(t_n), t_n) = &-\theta\frac{\Delta t}{\lambda}\big[f_\alpha(\tilde{\mathbf{x}}(t_{n+1}), t_{n+1}) - f_\alpha^{eq}(\tilde{\mathbf{x}}(t_{n+1}), t_{n+1})\big] \\ &- (1-\theta)\frac{\Delta t}{\lambda}\big[f_\alpha(\tilde{\mathbf{x}}(t_n), t_n) - f_\alpha^{eq}(\tilde{\mathbf{x}}(t_n), t_n)\big], \end{aligned} \tag{8}$$

where $t_{n+1} = t_n + \Delta t$, $\tilde{\mathbf{x}}(t_{n+1}) = \tilde{\mathbf{x}}(t_n) + \Delta t \mathbf{e}_\alpha$ and $\theta \in [0, 1]$. To obtain a second-order approximation one must choose $\theta = 1/2$.

Equation (8) can be solved very efficiently on the regular, structured mesh that coincides with the underlying lattice. For instance, with $\theta = 0$ Eq. (8) reduces to the conventional lattice Boltzmann equation

$$f_\alpha(\tilde{\mathbf{x}}(t_{n+1}), t_{n+1}) - f_\alpha(\tilde{\mathbf{x}}(t_n), t_n) = -\frac{\Delta t}{\lambda}\big[f_\alpha(\tilde{\mathbf{x}}(t_n), t_n) - f_\alpha^{eq}(\tilde{\mathbf{x}}(t_n), t_n)\big]. \tag{9}$$

To maintain second-order accuracy, one must choose $\nu = (\lambda/\Delta t - 0.5)c_s^2 \Delta t$ to account for the leading order truncation error in the Chapman–Enskog expansion. If we are to solve Eq. (8) on the unstructured mesh in complex geometries, however, we need to make use of the local approximation for $f_\alpha(\tilde{\mathbf{x}}(t_n), t_n)$ with $f_\alpha(\mathbf{x}_{ref}, t_n)$ at the expense of computational efficiency. Although $\mathbf{x}_{ref}$ is completely arbitrary between $\tilde{\mathbf{x}}(t_n)$ and $\tilde{\mathbf{x}}(t_{n+1})$, we choose $\mathbf{x}_{ref} = \tilde{\mathbf{x}}(t_{n+1})$ since it introduces some additional terms that enhance the stability of the numerical scheme [16]. From the geometrical point of view, we move backward relative to the particle followed. A simple one-dimensional, characteristic Galerkin procedure is illustrated in Fig. 2.

$$\tilde{\mathbf{x}}(t_n) = \tilde{\mathbf{x}}(t_{n+1}) - \Delta t \mathbf{e}_\alpha = \mathbf{x}_{ref} - \Delta t \mathbf{e}_\alpha \tag{10}$$

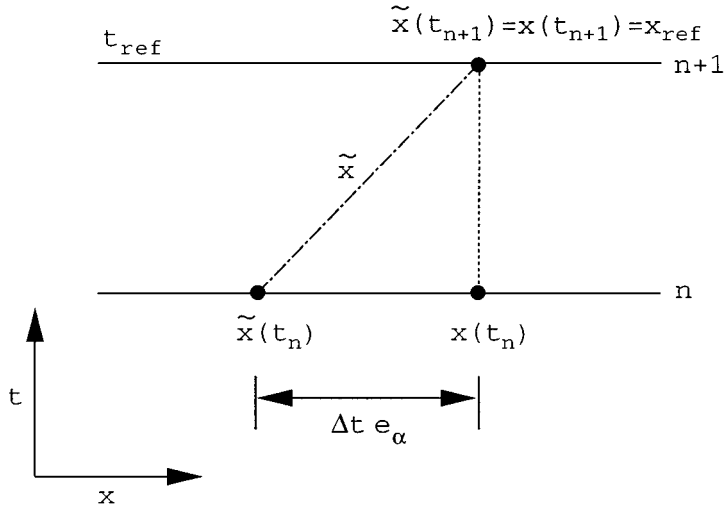

FIG. 2. A simple one-dimensional characteristic Galerkin procedure.

and therefore

$$f_\alpha(\tilde{\mathbf{x}}(t_n), t_n) = f_\alpha(\mathbf{x}_{ref} - \Delta t \mathbf{e}_\alpha, t_n)$$
$$= f_\alpha^n - \Delta t e_{\alpha r} \frac{\partial f_\alpha^n}{\partial x_r} + \frac{\Delta t^2}{2} e_{\alpha r} e_{\alpha s} \frac{\partial}{\partial x_s} \frac{\partial f_\alpha^n}{\partial x_r} + O(\Delta t^3), \tag{11}$$

where $f_\alpha^n = f_\alpha(\mathbf{x}_{ref}, t_n)$, $\mathbf{e}_\alpha = (e_{\alpha 1}, e_{\alpha 2})$, and summation is applied to the repeated indices r and s. An expression for $f_\alpha^{eq}(\tilde{\mathbf{x}}(t_n), t_n)$ is obtained in the same manner. Using Eq. (11) to approximate the terms in Eq. (8) with $\theta = 1/2$ and neglecting higher order terms give

$$f_\alpha^{n+1} - f_\alpha^n = -\Delta t \left[e_{\alpha r} \frac{\partial f_\alpha^n}{\partial x_r} + \frac{1}{\lambda} \left(f_\alpha - f_\alpha^{eq} \right)^{n+1/2} \right]$$
$$+ \frac{\Delta t^2}{2} e_{\alpha s} \frac{\partial}{\partial x_s} \left[e_{\alpha r} \frac{\partial f_\alpha^n}{\partial x_r} + \frac{1}{\lambda} \left(f_\alpha - f_\alpha^{eq} \right)^n \right] + O(\Delta t^3). \tag{12}$$

Although $f_\alpha^{n+1/2}$ in Eq. (12) can easily be approximated (e.g., by the Crank–Nicolson method), the equilibrium distribution function $f_\alpha^{eq,n+1/2}$ does not permit such an easy treatment. There are several options to approximate $f_\alpha^{eq,n+1/2}$. One can approximate $f_\alpha^{eq,n+1/2}$ by $f_\alpha^{eq,n}$ and $f_\alpha^{n+1/2}$ by f_α^n in spite of the severe stabilily limit caused by small λ. If $f_\alpha^{n+1/2}$ is approximated by f_α^{n+1} and $f_\alpha^{eq,n+1}$ by $f_\alpha^{eq,n}$, the stability limit may be overcome but a noticeable phase lag is observed. Mei and Shyy [12] proposed an extrapolation method that uses f_α^{eq} at time t_n and t_{n-1}. As they pointed out, however, the extrapolation method for f_α^{eq} is subject to numerical instability. In order to prevent the instability introduced by the extrapolation and circumvent the stability limit imposed by the relaxation term, we present the second-order accurate predictor-corrector method.

In the predictor step, we approximate $f_\alpha^{n+1/2}$ by f_α^{n+1} and $f_\alpha^{eq,n+1/2}$ by $f_\alpha^{eq,n}$. The gain is that the stability of the CGDBE is now mainly up to the convection stability limit known as the CFL condition because of the implicit treatment of f_α in the relaxation term. The

loss is that f_α after a predictor step suffers a phase lag so that it might not lie at time t_{n+1}, but somewhere between times t_n and t_{n+1}. This f_α, however, is found to serve as a good approximation to $f_\alpha^{n+1/2}$.

The predictor-corrector method can be expressed as follows.

- Predictor Step

$$\hat{f}_\alpha - f_\alpha^n = -\Delta t\left[e_{\alpha r}\frac{\partial f_\alpha^n}{\partial x_r} + \frac{1}{\lambda}\left(\hat{f}_\alpha - f_\alpha^{eq,n}\right)\right] + \frac{\Delta t^2}{2}e_{\alpha s}\frac{\partial}{\partial x_s}\left[e_{\alpha r}\frac{\partial f_\alpha^n}{\partial x_r} + \frac{1}{\lambda}\left(f_\alpha - f_\alpha^{eq}\right)^n\right]. \tag{13}$$

Here $\hat{f}_\alpha$ is taken as an approximation of $f_\alpha^{n+1/2}$ which represents some average value between times t_n and t_{n+1}. Likewise, $f_\alpha^{eq,n+1/2}$ can be approximated as

$$f_\alpha^{eq,n+1/2} \approx \hat{f}_\alpha^{eq} = w_\alpha\hat{\rho}\left[1 + 3(\mathbf{e}_\alpha\cdot\hat{\mathbf{u}}) + \frac{9}{2}(\mathbf{e}_\alpha\cdot\hat{\mathbf{u}})^2 - \frac{3}{2}(\hat{\mathbf{u}}\cdot\hat{\mathbf{u}})\right], \tag{14}$$

where $\hat{\rho} = \sum_{\alpha=0}^{8}\hat{f}_\alpha$ and $\hat{\rho}\hat{\mathbf{u}} = \sum_{\alpha=1}^{8}\mathbf{e}_\alpha\hat{f}_\alpha$.

- Corrector Step

$$f_\alpha^{n+1} - \hat{f}_\alpha = -\frac{\Delta t}{\lambda}\left(f_\alpha^{eq,n} - \hat{f}_\alpha^{eq}\right). \tag{15}$$

Numerical experiments show that this predictor-corrector method does not suffer from the phase lag which plagues Eq. (13).

We now apply the Galerkin finite element method to Eq. (13). Suppose that the domain Ω is discretized into an appropriate collection of finite elements, which are bilinear quadrilateral or triangular elements in the present study. The weak form of Eq. (13) is derived by multiplying it with the weighting function and integrating over the spatial domain of the problem. Let H^1 denote the Sobolev space of vector functions defined on the spatial domain Ω. We then perform integration by parts on the terms introduced by the characteristic Galerkin procedure and apply the divergence theorem. Since Eq. (13) is derived from a self-adjoint problem in space, the spatial discretization by the Galerkin method is optimal.

The Galerkin approximation is to find an approximate solution $f_\alpha^{(h)}$ of the following form in a finite dimensional subspace H^h of the space H^1.

$$f_\alpha^{(h)} = \mathbf{N}^T\mathbf{f}_\alpha, \tag{16}$$

where $\mathbf{N}^T = \{N^1, N^2, \ldots, N^{n_e}\}$ is a $(1\times n_e)$ vector of interpolation functions of the element Ω^e, the superscript $(\cdot)^T$ denotes the transpose operation, and n_e is the number of nodal points in an element. $\mathbf{f}_\alpha$ is a $(n_e\times 1)$ vector of nodal particle distribution functions. Likewise, $f_\alpha^{eq,(h)} = \mathbf{N}^T\mathbf{f}_\alpha^{eq}$ for the equilibrium function.

By applying the Galerkin method to Eq. (13) and expressing Eq. (15) in vector form, one obtains

- Predictor Step

$$\mathbf{M}\left(\hat{\mathbf{f}}_\alpha - \mathbf{f}_\alpha^n\right) = -\Delta t\left\{\mathbf{C}_\alpha\mathbf{f}_\alpha^n + \frac{1}{\lambda}\mathbf{M}\left(\hat{\mathbf{f}}_\alpha - \mathbf{f}_\alpha^{eq,n}\right) + \Delta t\left[\mathbf{D}_\alpha\mathbf{f}_\alpha^n + \mathbf{Q}_\alpha\left(\mathbf{f}_\alpha^n - \mathbf{f}_\alpha^{eq,n}\right)\right]\right\}. \tag{17}$$

- Corrector Step

$$\mathbf{f}_\alpha^{n+1} - \hat{\mathbf{f}}_\alpha = -\frac{\Delta t}{\lambda}\left(\mathbf{f}_\alpha^{eq,n} - \hat{\mathbf{f}}_\alpha^{eq}\right), \tag{18}$$

where $(n_e \times n_e)$ matrices $\mathbf{M}$, $\mathbf{C}_\alpha$, $\mathbf{D}_\alpha$, and $\mathbf{Q}_\alpha$ are defined as

$$\mathbf{M} = \int_{\Omega^e} \mathbf{N}\mathbf{N}^T \, d\Omega, \tag{19}$$

$$\mathbf{C}_\alpha = \int_{\Omega^e} \mathbf{N} e_{\alpha r} \frac{\partial \mathbf{N}^T}{\partial x_r} \, d\Omega, \tag{20}$$

$$\mathbf{D}_\alpha = -\frac{1}{2}\int_{\Omega^e} \mathbf{N} e_{\alpha r} e_{\alpha s} \frac{\partial^2 \mathbf{N}^T}{\partial x_s \partial x_r} \, d\Omega, \tag{21}$$

$$\mathbf{Q}_\alpha = -\frac{1}{2\lambda}\int_{\Omega^e} \mathbf{N} e_{\alpha s} \frac{\partial \mathbf{N}^T}{\partial x_s} \, d\Omega. \tag{22}$$

$\mathbf{D}_\alpha$ and $\mathbf{Q}_\alpha$ are introduced by the discretization along the characteristics and help to stabilize Eq. (17). In general, one integrates Eq. (21) by parts and applies the divergence theorem of Gauss to obtain

$$\mathbf{D}_\alpha = \frac{1}{2}\left(\int_{\Omega^e} \frac{\partial \mathbf{N}}{\partial x_s} e_{\alpha s} e_{\alpha r} \frac{\partial \mathbf{N}^T}{\partial x_r} d\Omega - \oint_{\Gamma^e} \mathbf{N} n_s e_{\alpha s} e_{\alpha r} \frac{\partial \mathbf{N}^T}{\partial x_r} d\Gamma\right), \tag{23}$$

where Γ^e denotes the surface of elements and n_s are the components of the outward vector normal to Γ. The second term on the right-hand side is the surface integral and cancels out in the interior of the domain Ω. It is noteworthy that the first term on the right-hand side of Eq. (23) multiplied by Δt^2 is identical in form to the balancing tensor diffusivity (BTD) [20] and is similar to the streamline upwind term [24]. The BTD is to compensate the truncation error of the pure advection equation discretized by the forward Euler method, and the streamline upwind term is to add optimal diffusion to the governing equation in the streamline direction. Exclusion of the term associated with $\mathbf{Q}_\alpha$ from Eq. (17) tends to result in excessive numerical diffusion, and thus lower Reynolds number flows. With none of these terms, the method is likely to be unstable.

2.3. *Boundary Condition*

The surface integrals in Eq. (23) in the interior of the domain cancel out and those at the domain boundary remain to be determined by boundary conditions. For the essential boundary condition, Eqs. (17) and (18) at the boundary nodes are dropped and replaced by the prescribed f_α values. If the boundary condition is natural, the normal flux associated with the surface integral in Eq. (23) is specified. For the CGDBE and LBE methods, however, neither essential or natural boundary conditions seem to be appropriate because usually boundary conditions are given for macroscopic variables, such as fluid velocities, pressure, or their gradients, but not for particle distribution functions.

Several attempts to reconstruct boundary f_α^{n+1} from the constraints in Eq. (5) have been made [25–28]. Nevertheless, it is not easy to generalize these boundary conditions for the use of complex geometries and three-dimensional problems. The widely used bounce-back scheme and equilibrium boundary condition are easy to implement, but are of lower order

accuracy [29]. Chen *et al.* [30] and Mei and Shyy [12] took an alternative approach that can preserve the overall order of accuracy of the LBE methods. In the extrapolation scheme of Chen *et al.* [30], the values of f_α^n at the fictitious nodes adjacent to the boundary nodes are obtained by linear extrapolation prior to the streaming step. In the finite difference-based LBE method in body-fitted coordinates, Mei and Shyy [12] used the one-sided difference scheme to approximate the gradients of f_α^n at the boundary nodes and demonstrated that the extrapolation scheme leads to the one-sided difference at the boundary nodes. In both schemes, macroscopic boundary conditions are incorporated through f_α^{eq} and the LBEs at the boundary nodes are solved for f_α^{n+1} at the domain boundary.

This approach is akin to the "no" boundary condition that is used as an outflow boundary condition in finite element methods [20, 30–34]. The idea of "no" boundary condition is simply not to perform integration by parts on the equations associated with the boundary nodes because "no" information on variables at time t_{n+1} is used. Thus construction of Eq. (17) at the boundary nodes only involves the elements adjacent to the boundary nodes and f_α^n without any assumptions on f_α^{n+1} and its gradient, similar to the above extrapolation scheme and one-sided difference approximation. But a major difference between the original "no" boundary condition and its application to the CGDBE is that the latter permits macroscopic boundary conditions to be reflected through f_α^{eq} while mesoscopic boundary conditions for f_α^{n+1} remain unspecified.

Numerical experiments by [12, 30] and those to be presented later show that the approach, which treats f_α^{n+1} at the domain boundary as part of the solution and imposes physical boundary conditions through f_α^{eq}, can be applied to stationary/moving walls and inlet/outlet boundaries. The physical Neumann boundary condition can also be implemented by assigning the updated values of macroscopic variables at the interior nodes next to the domain boundary to the boundary nodes in the direction that the Neumann condition is applied. Interpolation is required if the grid lines near the domain boundary are not parallel to the direction of the Neumann condition.

2.4. *Accuracy and Stability*

As shown in Section 2.2, the present CGDBE scheme is of second-order accuracy in time. However, the spatial accuracy depends on the shape of interpolation functions. For a piecewise linear shape function, it can be shown that transient solutions for the pure advection equation on uniform meshes enjoy fourth-order spatial accuracy and zero numerical diffusion (see Appendix). The relaxation term has no effect on the spatial accuracy.

Equation (17) is only conditionally stable because the convection term is treated explicitly. The stability condition for pure convection problems with linear elements is given as [16, 35]

$$\Delta t_{conv} \le \frac{h}{3|\mathbf{e}|}, \tag{24}$$

where $\mathbf{e}$ is the discrete velocity in the characteristic direction and h is the element size in that direction.

3. RESULTS

In this section we present several test cases and compare with previous analytical and numerical results. Unsteady Couette flow, lid-driven cavity flow, and steady flow past a

circular cylinder will be examined. For all cases, the boundary condition is imposed through f_α^{eq} with the prescribed velocity as described in Section 2.3.

3.1. *Unsteady Couette Flow*

In order to evaluate the temporal accuracy of the CGDBE, we examine unsteady Couette flow. The top plate moves at a constant velocity, $\mathbf{u} = (U, 0)$ and the bottom one is kept stationary. A periodic boundary condition is applied in the x-direction. Mach number Ma is 0.1 and the velocity of the top plate is calculated by the relation $U = c_s$ Ma. The fluid density ρ is 1.0 and the Reynolds number $\mathrm{Re} = \frac{UL}{\nu}$ is 10, where L is the channel width. The Navier–Stokes equation for this simple two-dimensional parallel flow reduces to

$$\frac{\partial u(y,t)}{\partial t} = \nu \frac{\partial^2 u(y,t)}{\partial y^2}. \tag{25}$$

The analytical solution of this equation is

$$u(y,t) = U\frac{y}{L} + \sum_{m=1}^{\infty} \frac{2U(-1)^m}{\lambda_m L} e^{-\nu\lambda_m^2 t} \sin \lambda_m y, \tag{26}$$

where $\lambda_m = \frac{m\pi}{L}$, $m = 1, 2, 3 \ldots$.

Figure 3 shows a series of normalized velocity profiles at different times for this flow. The solid lines represent the analytical solution and the circles represent the CGDBE results obtained using 20 elements in the y-direction. The numerical solutions are in excellent agreement with the analytic counterparts.

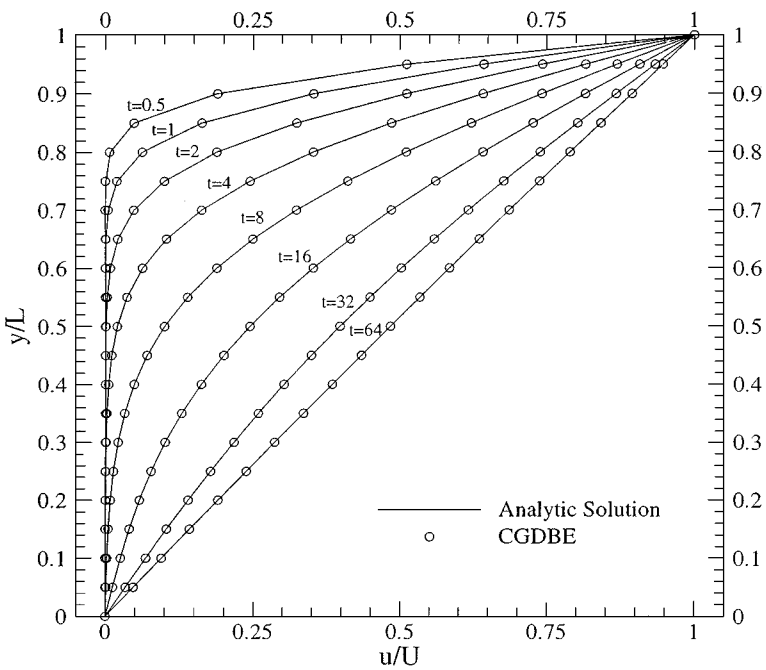

FIG. 3. Normalized velocity profiles across the normalized channel width at different times.

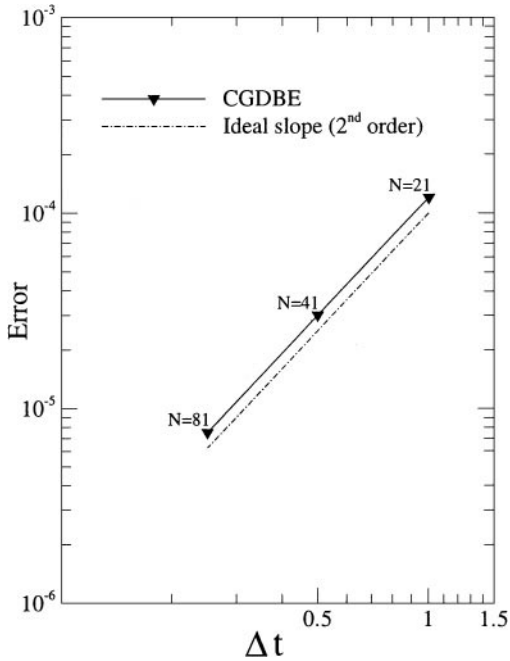

FIG. 4. The error as a function of time step.

For calculation of the temporal accuracy, 20, 40, and 80 uniform bilinear quadrilateral elements are used in the y-direction. Both time step and Mach number are systematically reduced as the mesh size decreases with a constant CFL number and a $\Delta t/\mathrm{Ma}$ ratio. The following average error measure is used.

$$\epsilon = \frac{\sum_i \left| u_i^{analytic} - u_i^{CGDBE} \right|}{N}, \tag{27}$$

where N is the number of grid points in the y-direction. The error is plotted against normalized time step ($\Delta t = 1$ for the largest time step) in Fig. 4. The CGDBE error curve follows the slope of the second-order scheme.

3.2. *Lid-Driven Cavity Flow*

Although the simulation of lid-driven cavity flow is a well-known benchmark problem, it is not a trivial one because of the difficulty in capturing flow phenomena near numerical singularities at the top corners of the cavity. Therefore, it is desirable to refine the mesh near those singular points. The reasons for choosing lid-driven cavity flow as a test problem are to evaluate the spatial accuracy of the CGDBE at steady state and to demonstrate advantages of using nonuniform meshes.

3.2.1. Spatial accuracy evaluation at $Re = 400$. The Reynolds number is defined as $\mathrm{Re} = UL/\nu$, where U is the velocity of the top lid and L is the length of the top lid. The solutions are obtained using $\mathrm{Ma} = 0.1$, $L = 1.0$, and $\rho = 1.0$. The equilibrium distribution

function is used to specify initial conditions. The convergence criterion is

$$\frac{\sum_i \left|\phi_i^n - \phi_i^{n-1}\right|}{N} < \epsilon, \tag{28}$$

where N denotes the total number of nodes, the superscript n denotes the time level, ϕ is any macroscopic variable, and ϵ is the error criterion set to $1.0e-7$ in the present study.

In order to demonstrate the spatial accuracy of the CGDBE, calculations are performed on three systematically refined uniform meshes using 64×64, 128×128, and 256×256 rectangular elements (denoted by the subscripts $4h$, $2h$, and h, respectively). Since the ratio of the mesh size on successive meshes is 2, the order of the scheme, p, can be estimated as follows [36].

$$p = \frac{\ln\left(\frac{\phi_{2h} - \phi_{4h}}{\phi_h - \phi_{2h}}\right)}{\ln 2}. \tag{29}$$

This leads to $p = 2.1$, confirming that the spatial accuracy of the CGDBE is of second order for the steady state solution.

3.2.2. Nonuniform mesh calculation. Using a 65×65 nonuniform mesh, calculations are performed for $\mathrm{Re} = 400$, $\mathrm{Re} = 1000$, $\mathrm{Re} = 3200$, and $\mathrm{Re} = 5000$. For all cases $\mathrm{Ma} = 0.1$, $L = 1.0$, and $\rho = 1.0$. Figures 5–7 show contour plots of stream function, vorticity, and

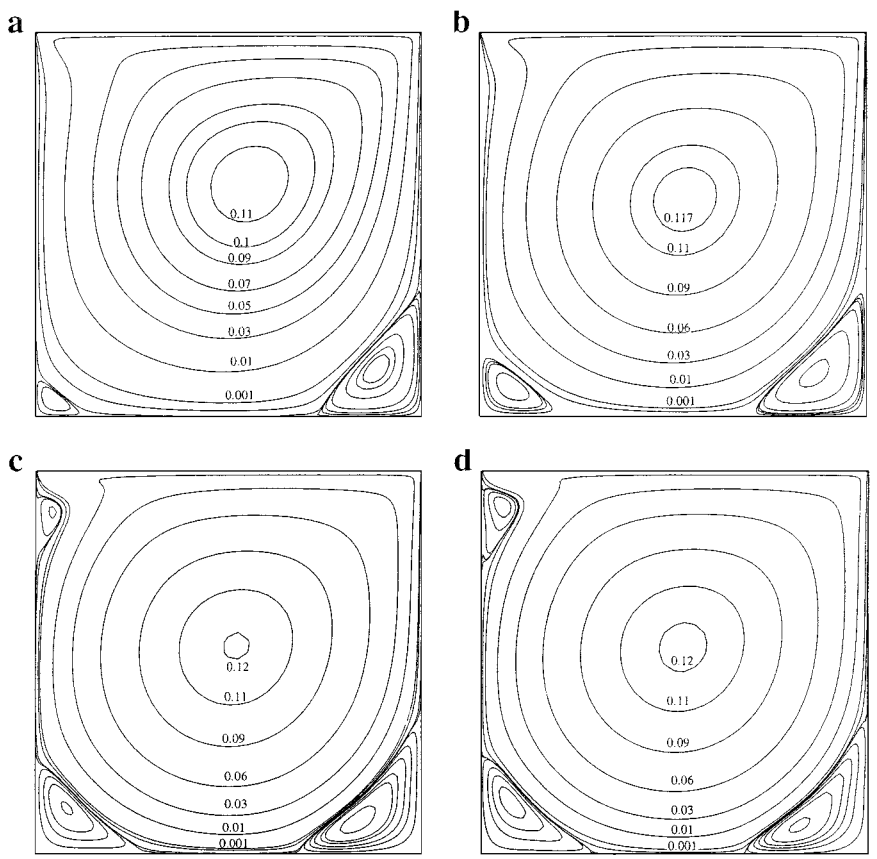

FIG. 5. Stream functions of the cavity flow: (a) $\mathrm{Re} = 400$; (b) $\mathrm{Re} = 1000$; (c) $\mathrm{Re} = 3200$; (d) $\mathrm{Re} = 5000$.

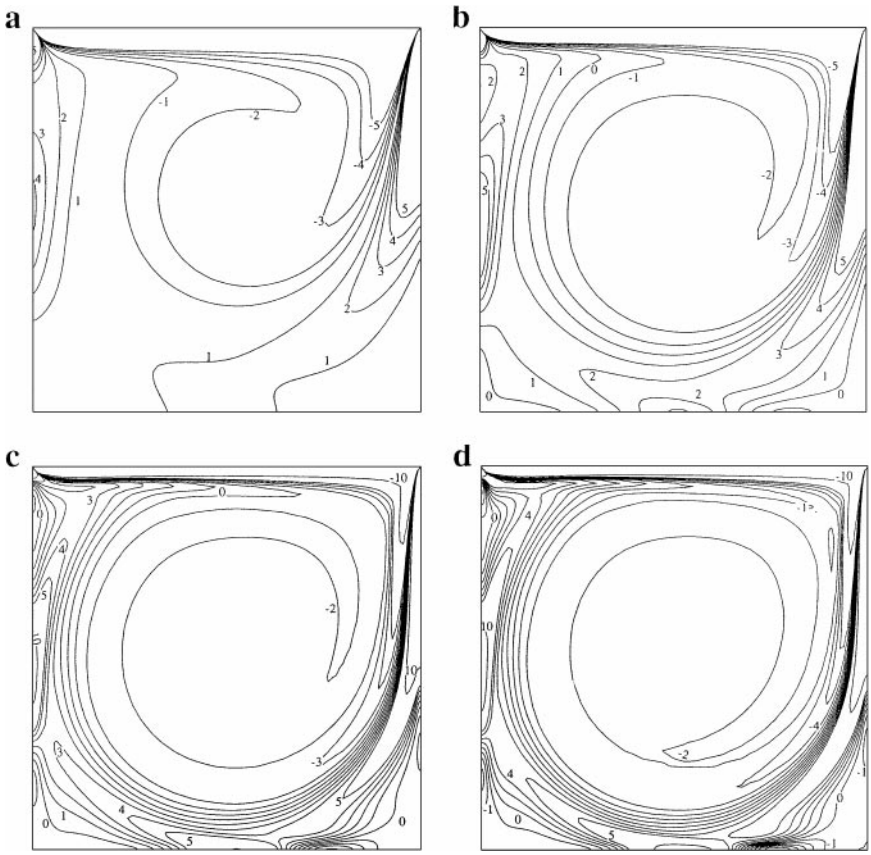

FIG. 6. Vorticity contours of the cavity flow: (a) Re = 400; (b) Re = 1000; (c) Re = 3200; (d) Re = 5000.

pressure, respectively. The flow structure is in good agreement with previous results of Ghia *et al.* [37]. Comparison of the profiles of the horizontal velocity component in the vertical symmetry plane is shown in Fig. 8. Table I lists the locations and values of stream function for the vortices. The results of Ghia *et al.* [37] and Hou *et al.* [29] are also displayed for comparison. The results obtained from the nonuniform mesh indicate that the CGDBE can simulate finite Reynolds number flow problems with fewer grid points than the LBE method.

To emphasize this point, we compare the results using the CGDBE and the conventional LBE method [38] at Re = 400 and Ma = 0.1 with the same number of grid points on coarse meshes. Boundary and initial conditions for the CGDBE are given as above, and a 33×33 nonuniform mesh is used. For the LBE method, the complete bounce-back rule is applied at the stationary walls and the equilibrium boundary condition is applied to the top wall. A 33×33 uniform mesh is used for the LBE method. Figures 9 and 10 show the velocity vectors and the pressure contours obtained from both methods. The CGDBE seems to generate better results than the LBE method. Due to the lack of grid points, the LBE method yields oscillatory velocities near the upper left corner of the cavity in Fig. 9b, which can be removed by the composite LBE method [38]. The pressure field calculated from the LBE method exhibits a severe checkerboard pattern. Profiles of the horizontal velocity component in the vertical symmetry plane are shown in Fig. 11. Again, the LBE method yields less accurate profile as well as the spurious slip velocity near the walls caused by the

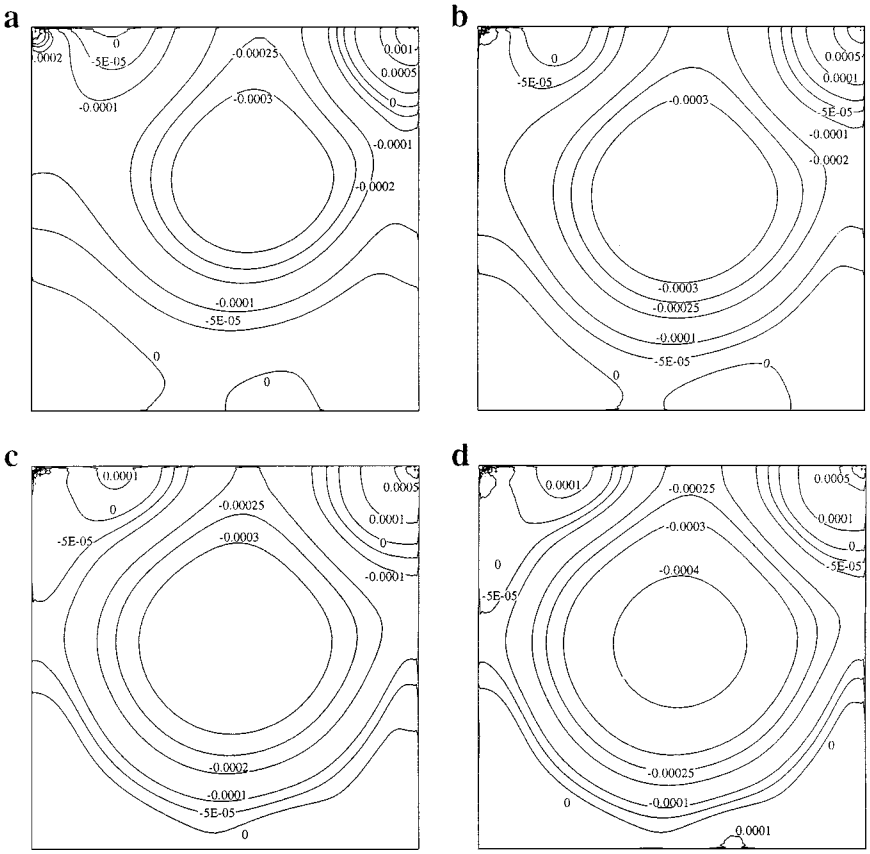

FIG. 7. Pressure contours of the cavity flow: (a) Re = 400; (b) Re = 1000; (c) Re = 3200; (d) Re = 5000.

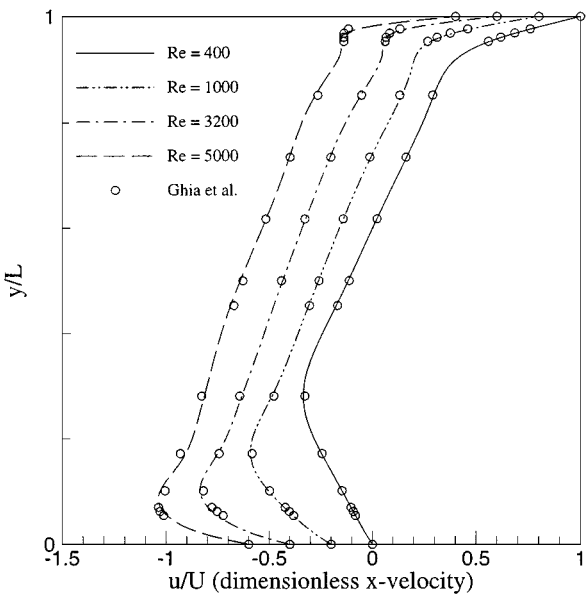

FIG. 8. Profiles of normalized velocity component *u* through the geometric center of the cavity at various Reynolds numbers (profiles are shifted from the original location for comparison).

TABLE I
Locations and Values of Maximum and Minimum Stream Function for Three Vortices of the Lid-Driven Cavity Flows at Reynolds Numbers 400, 1000, 3200, 5000

		Primary vortex			Lower left vortex			Lower right vortex		
Re	Case	ψ_{max}	x/L_{lid}	y/L_{lid}	ψ_{min}	x/L_{lid}	y/L_{lid}	ψ_{min}	x/L_{lid}	y/L_{lid}
400	Ghia *et al.*[a]	0.1139	0.5547	0.6055	−1.42*e*−5	0.0508	0.0469	−6.42*e*−4	0.8906	0.1250
	Hou *et al.*[b]	0.1121	0.5608	0.6078	−1.30*e*−5	0.0549	0.0510	−6.19*e*−4	0.8902	0.1255
	present work[c]	0.1158	0.5516	0.6024	−1.32*e*−5	0.0529	0.0443	−6.82*e*−4	0.8799	0.1201
1000	Ghia *et al.*[d]	0.1179	0.5313	0.5625	−2.31*e*−4	0.0859	0.0781	−1.75*e*−3	0.8594	0.1094
	Hou *et al.*[b]	0.1178	0.5333	0.5647	−2.22*e*−4	0.0902	0.0784	−1.69*e*−3	0.8667	0.1137
	present work[c]	0.1204	0.5259	0.5771	−2.26*e*−4	0.0830	0.0830	−1.76*e*−3	0.8658	0.1069
3200	Ghia *et al.*[d]	0.1204	0.5165	0.5469	−9.78*e*−4	0.0859	0.1094	−3.14*e*−3	0.8125	0.0859
	present work[c]	0.1206	0.5259	0.5516	−1.16*e*−3	0.0830	0.1200	−3.02*e*−3	0.8349	0.0830
5000	Ghia *et al.*[a]	0.1190	0.5117	0.5352	−1.36*e*−3	0.0703	0.1367	−3.08*e*−3	0.8086	0.0742
	Hou *et al.*[b]	0.1214	0.5176	0.5373	−1.35*e*−3	0.0784	0.1373	3.03*e*−3	0.8078	0.0745
	present work[c]	0.1217	0.5259	0.5516	−1.49*e*−3	0.0722	0.1342	−3.47*e*−3	0.8181	0.0722

[a] 257 × 257 uniform mesh.
[b] 257 × 257 lattice nodes.
[c] 65 × 65 nonuniform mesh.
[d] 129 × 129 uniform mesh.

lower order boundary conditions, such as the complete bounce-back rule and the equilibrium boundary condition.

3.3. *Steady Flow past a Circular Cylinder at Re = 20*

We consider laminar steady flow past a circular cylinder on both structured and unstructured meshes. The flow behind a circular cylinder remains symmetric up to Re =

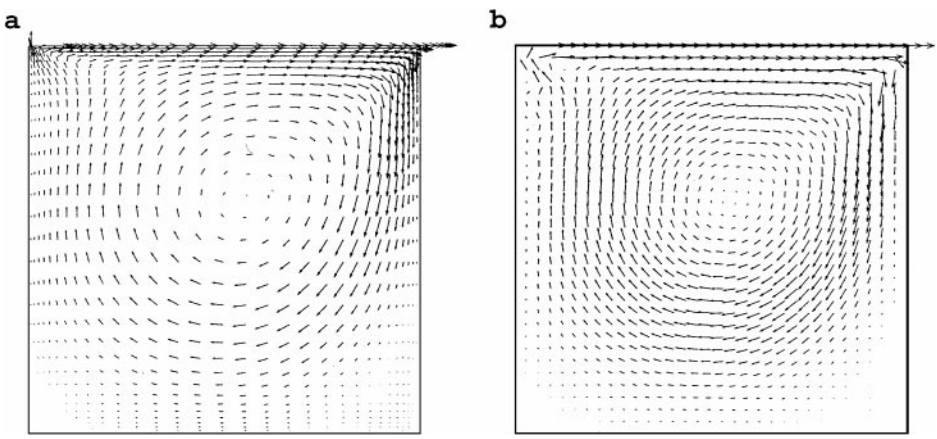

FIG. 9. Velocity vectors of the cavity flow at Re = 400: (a) CGDBE; (b) LBE.

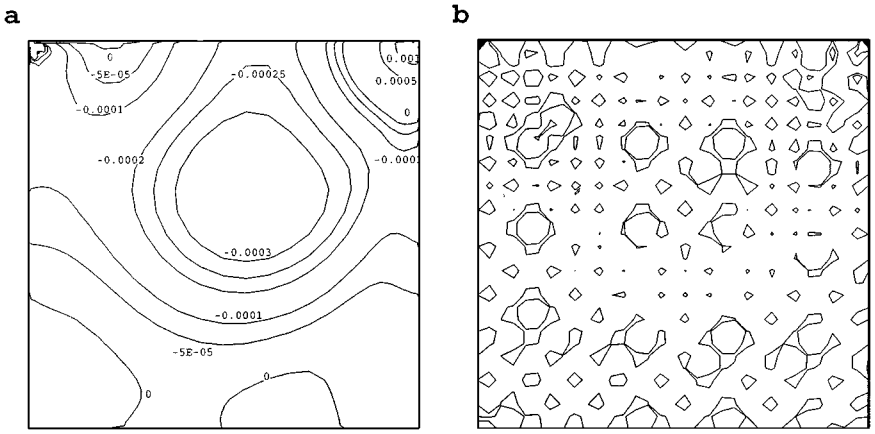

FIG. 10. Pressure contours of the cavity flow at Re = 400: (a) CGDBE; (b) LBE.

$(2u_\infty r_0)/\nu \approx 40$, where u_∞ is the free stream velocity and r_0 is the cylinder radius. At a Reynolds number of 20, a steady recirculation bubble is attached to the cylinder surface.

The structured mesh is generated in $r-\theta$ cylindrical coordinates. The stretching formula in the r-direction is given as [12]

$$r = r_0 + (r_\infty - r_0)\left\{1 - \frac{1}{\beta}\arctan[(1-\eta)\tan(\beta)]\right\}, \tag{30}$$

where r_∞ is the domain radius. $\eta = (i-1)/(n_r - 1)$, where i and n_r are the grid index

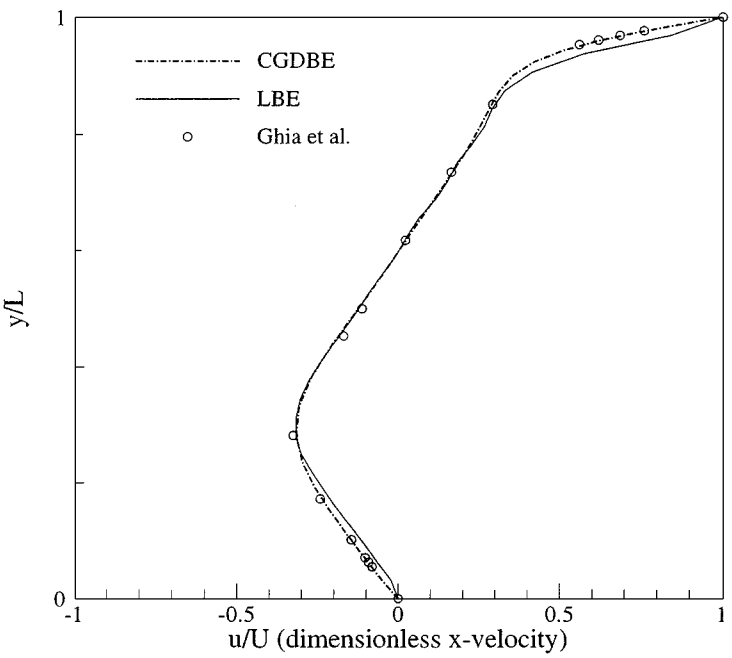

FIG. 11. Profiles of normalized velocity component u through the geometric center of the cavity at Re = 400 and Ma = 0.1 with 33 × 33 grid points.

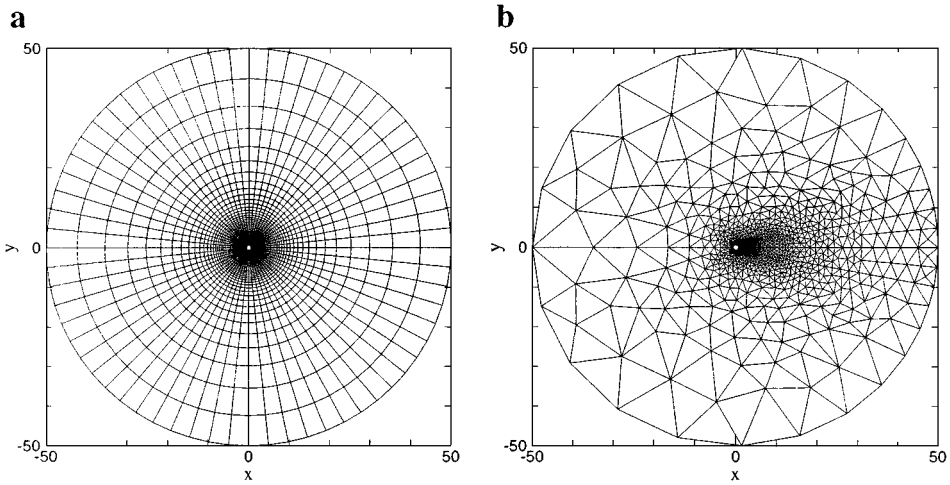

FIG. 12. (a) Structured mesh with 129×64 grid points, (b) unstructured mesh with 2568 grid points.

and grid number in the r-direction. For the present calculations, $r_0 = 0.5$, $r_\infty = 50$, $\beta^{-1} = 0.65$, as used by Mei and Shyy [12]. Also, Ma $= 0.1$, and Re $= 20$. At the inlet and outflow boundaries, the uniform velocity $\mathbf{u} = (u_\infty, 0)$ is imposed as the boundary condition. Intervals of 128 and 64 in the respective r and θ directions are used. The unstructured mesh is composed of hybrid elements. Bilinear quadrilateral elements are used near the cylinder wall to capture the boundary layer, and bilinear triangular elements are used elsewhere since quadrilateral elements are better suited to the boundary-layer type flow and triangular elements are quite adaptable for mesh clustering and coarsening. The number of grid points along the cylinder wall is 64 and the total numbers of grid points and elements are 2568 and 4276, respectively. Figure 12 shows structured and unstructured mesh setups. The ratio of the CPU time required per time step of the structured mesh calculation with 129×64 (8256) grid points to that of the unstructured mesh calculation with 2568 grid points is about 4.7 on the HP 9000/785 workstation. The increase in the CPU time for structured mesh calculation is due to the increase in the number of grid points and the number of neighbor nodes connected. Time steps are 0.004 for all cases and the steady-state solutions are reached after 200,000 iterations.

Table II lists the quantitative geometrical parameters in the wake region. The length of the wake region, L, is defined as the distance between the rearmost point of the cylinder and the end of the wake. The separation angle, θ_s, is the angle between the rearmost point and the point where the separation occurs. Both parameters agree well with the results of previous studies. Note that the results of the unstructured mesh calculation agree well with those of the structured mesh calculation in spite of fewer grid points. Table III lists the quantitative comparisons for the drag coefficient (C_D), and the stagnation pressure coefficients at the front ($C_p(\pi)$) and the end ($C_p(0)$) of the cylinder. The drag coefficient is calculated as

$$C_D = \frac{1}{\rho u_\infty^2 r_0} \oint_{\Gamma_c} S_{ij} n_j \, d\Gamma, \tag{31}$$

where n_j are the components of the outward normal vector on the cylinder wall, Γ_c denotes

TABLE II
Comparison of Geometrical Parameters for the Flow past a Circular Cylinder at Re = 20

Authors	L/a	θ_s
Tritton[a] (1959)	1.86	41.6
Dennis and Chang[b] (1970)	1.88	43.7
Nieuwstadt and Keller[b] (1973)	1.786	43.37
Fornberg[b] (1980)	1.82	—
Mei and Shyy[c] (1997)	1.804	42.1
He and Doolen[d] (1997)	1.842	42.96
Present work[e]	1.846	43.35
Present work[f]	1.85	44.08

[a] Experiment.
[b] Numerical simulation of Navier–Stokes equations.
[c] FDLBM with 129×64 grid points.
[d] ISLBE with 181×241 grid points.
[e] Structured mesh with 129×64 grid points.
[f] Unstructured mesh with 2568 grid points.

the cylinder surface, and

$$S_{ij} = -p\delta_{ij} + \rho\nu\left(\frac{\partial u_i}{\partial x_j} + \frac{\partial u_j}{\partial x_i}\right) \tag{32}$$

is the stress tensor. For the drag force in the streamwise direction, the subscript i is taken as one. The pressure coefficient is defined as

$$C_p = \frac{p - p_\infty}{\frac{1}{2}\rho u_\infty^2}. \tag{33}$$

As shown in Table III, the drag and pressure coefficients are in good agreement with results of previous studies.

TABLE III
Comparison of Dynamical Parameters for the Flow past a Circular Cylinder at Re = 20

Authors	C_D	$C_p(\pi)$	$-C_p(0)$
Dennis and Chang[a] (1970)	2.045	1.269	0.589
Nieuwstadt and Keller[a] (1973)	2.053	1.274	0.582
Fornberg[a] (1980)	2.000	1.28	0.54
He and Doolen[b] (1997)	2.152	1.233	0.567
Present work[c]	2.030	1.256	0.593
Present work[d]	1.998	1.248	0.530

[a] Numerical simulation of Navier–Stokes equations.
[b] ISLBE with 181×241 grid points.
[c] Structured mesh with 129×64 grid points.
[d] Unstructured mesh with 2568 grid points.

4. CONCLUSIONS

The characteristic Galerkin finite element method has been successfully applied to solving the discrete Boltzmann equation. Due to the inherent geometrical flexibility of the finite element method, flows in complex geometries can be easily simulated. In addition, the use of unstructured meshes increases the numerical accuracy while reducing the computational cost. In order to circumvent the stability limit arising from the relaxation term, the predictor-corrector method is proposed.

Unsteady Couette flow, lid-driven cavity flow, and steady flow past a circular cylinder are chosen as test cases. Numerical results confirm the theoretically estimated numerical accuracy of the CGDBE. Good agreement of the results from the CGDBE with the analytical (if applicable), experimental, and previous numerical results indicates that the CGDBE extends the applicability of the traditional LBE method to flows in complex geometries.

APPENDIX

For a constant advection velocity e, the one-dimensional pure advection equation for $f(x, t)$ can be written in the form

$$\frac{\partial f}{\partial t} = f_t = -e\frac{\partial f}{\partial x} = -ef_x \tag{A.1}$$

or

$$f(\tilde{\mathbf{x}}(t_{n+1}), t_{n+1}) - f(\tilde{\mathbf{x}}(t_n), t_n) = 0. \tag{A.2}$$

If we apply the local approximation Eq. (11) to Eq. (A.2), we obtain

$$f^{n+1} - f^n = -e\Delta t f_x^n - \frac{e^2\Delta t^2}{2} f_{xx}^n. \tag{A.3}$$

Equation (A.3) can be discretized using a Galerkin method. For a typical node i, using linear elements of equal size Δx, we obtain the assembled finite element equation

$$\begin{aligned}\frac{1}{6}\left[\left(f_{i-1}^{n+1} + 4f_i^{n+1} + f_{i+1}^{n+1}\right) - \left(f_{i-1}^n + 4f_i^n + f_{i+1}^n\right)\right] \\ = -\frac{e\Delta t}{2\Delta x}\left(f_{i+1}^n - f_{i-1}^n\right) + \frac{e^2\Delta t^2}{2\Delta x^2}\left(f_{i-1}^n + 2f_i^n + f_{i+1}^n\right).\end{aligned} \tag{A.4}$$

In order to determine the accuracy of the scheme, we will consider numerical representation of the modified transport equation following [35]

$$f_t + ef_x = a_{et} f_{xx} + \varepsilon_t^* = \varepsilon_t, \tag{A.5}$$

where a_{et} is the transient equivalent numerical diffusion, ε_t^* is the residual transient truncation error, and ε_t is the global transient truncation error.

Taylor series expansion of f around the time instant $t = n\Delta t$ and the grid point i in the x-coordinate is

$$
\begin{aligned}
&f(x \pm \Delta x, t + \Delta t) \\
&\quad = f(x,t) \pm \Delta x f_x(x,t) + \Delta t f_t(x,t) + \frac{\Delta x^2}{2} f_{xx}(x,t) \pm \Delta x \Delta t f_{xt}(x,t) + \frac{\Delta t^2}{2} f_{tt}(x,t) \\
&\qquad \pm \frac{\Delta x^3}{6} f_{xxx}(x,t) + \frac{\Delta x^2 \Delta t}{2} f_{xxt}(x,t) \pm \frac{\Delta x \Delta t^2}{2} f_{xtt}(x,t) + \frac{\Delta t^3}{6} f_{ttt}(x,t) + \cdots .
\end{aligned} \tag{A.6}
$$

Using Eq. (A.6) we obtain the general expression of the transient truncation error ε_t of Eq. (A.4) at the grid point i and the time level n

$$
\varepsilon_t = -\Delta t \left(\frac{1}{2} f_{tt} - \frac{e^2}{2} f_{xx} \right) - \frac{\Delta t^2}{6} f_{ttt} - \Delta x^2 \left(\frac{1}{6} f_{xxt} + \frac{e}{6} f_{xxx} \right) + O(\Delta t^3, \Delta x^4). \tag{A.7}
$$

Equation (A.7) can be rearranged by recursive application of the advection equations (A.1)

$$
f_{tt} = e^2 f_{xx}, \quad f_{xxt} = -e f_{xxx}, \quad f_{xtt} = e^2 f_{xxx}, \quad f_{ttt} = -e^3 f_{xxx}. \tag{A.8}
$$

Then, Eq. (A.7) becomes

$$
\begin{aligned}
\varepsilon_t &= -\Delta t \left(\frac{e^2}{2} f_{xx} - \frac{e^2}{2} f_{xx} \right) - \frac{\Delta t^2}{6} f_{ttt} + \Delta x^2 \left(\frac{e}{6} f_{xxx} - \frac{e}{6} f_{xxx} \right) + O(\Delta t^3, \Delta x^4) \\
&= O(\Delta t^2, \Delta x^4).
\end{aligned} \tag{A.9}
$$

The transient equivalent numerical diffusion, a_{et}, becomes identically zero and the residual transient truncation error, ε_t^*, is $O(\Delta t^2, \Delta x^4)$ on the regular, equally spaced mesh.

ACKNOWLEDGMENTS

This work was supported by the Carver Scientific Research Initiative Grants Program at the University of Iowa. The computing time was provided by the National Center for Atmospheric Research.

REFERENCES

1. S. Chen and G. D. Doolen, Lattice Boltzmann method for fluid flows, *Ann. Rev. Fluid Mech.* **30**, 329 (1998).
2. X. He and L.-S. Luo, A priori derivation of the lattice Boltzmann equation, *Phys. Rev. E.* **55**, R6333 (1997).
3. X. He and L.-S. Luo, Theory of the lattice Boltzmann method: From the Boltzmann equation to the lattice Boltzmann equation, *Phys. Rev. E.* **56**, 6811 (1997).
4. T. Abe, Derivation of the lattice Boltzmann method by means of the discrete ordinate method for the Boltzmann equation, *J. Comput. Phys.* **131**, 241 (1997).
5. O. Filippova and D. Hänel, Grid refinement for Lattice-Boltzmann models, *J. Comput. Phys.* **147**, 219 (1998).
6. R. Mei, L. Luo, and W. Shyy, An accurate curved boundary treatment in the lattice Boltzmann method, *J. Comput. Phys.* **155**, 307 (1999).
7. R. Mei, W. Shyy, D.Yu, and L. Luo, Lattice Boltzmann method for 3-D flows with curved boundary, *J. Comput. Phys.* **161**, 680 (2000).

8. X. He, L.-S. Luo, and M. Dembo, Some progress in lattice Boltzmann method. Part I. Nonuniform mesh grids, *J. Comput. Phys.* **129**, 357 (1996).
9. X. He and G. D. Doolen, Lattice Boltzmann method on a curvilinear coordinate system: Vortex shedding behind a circular cylinder, *Phys. Rev. E.* **56**, 434 (1997).
10. X. He and G. D. Doolen, Lattice Boltzmann method on curvilinear coordinates system: Flow around a circular cylinder, *J. Comput. Phys.* **134**, 306 (1997).
11. N. Cao, S. Chen, S. Jin, and D. Martínez, Physical symmetry and lattice symmetry in the lattice Boltzmann method, *Phys. Rev. E.* **E55**, R21 (1997).
12. R. Mei and W. Shyy, On the finite difference-based lattice Boltzmann method in curvilinear coordinates, *J. Comput. Phys.* **143**, 426 (1998).
13. S. Succi, G. Amati, and R. Benzi, Challenges in lattice Boltzmann computing, *J. Stat. Phys.* **81**, 5 (1995).
14. H. Xi, G. Peng, and S.-H. Chou, Finite-volume lattice Boltzmann method, *Phys. Rev. E.* **59**, 6202 (1999).
15. H. Xi, G. Peng, and S.-H. Chou, Finite-volume lattice Boltzmann schemes in two and three dimensions, *Phys. Rev. E.* **60**, 3380 (1999).
16. O. C. Zienkiewicz and R. Codina, A general algorithm for compressible and incompressible flow—Part I. The split, characteristic-based scheme, *Int. J. Numer. Methods Fluids* **20**, 869 (1995).
17. J. Donea, A Taylor–Galerkin method for convection transport problems, *Int. J. Numer. Methods Fluids* **4**, 1043 (1984).
18. O. C. Zienkiewicz and R. Taylor, *Finite Element Method*, 4th ed. (McGraw-Hill, New York, 1991), Vol. II.
19. P. D. Lax and B. Wendroff, Systems of conservation laws, *Comm. Pure Appl. Math.* **13**, 217 (1960).
20. P. M. Gresho and R. L. Sani, *Incompressible Flow and the Finite Element Method* (Wiley, New York, 1998).
21. T. Matsushita, *Study of Evaporation and Condensation Problems by Kinetic Theory*, Institute of Space and Astronautical Science, University of Tokyo Report 541, 1976.
22. P. L. Bhatnagar, E. P. Gross, and M. Krook, A model for collision processes in gases. I. Small amplitude processes in charged and neutral one-component system, *Phys. Rev.* **94**, 511 (1954).
23. D. Wolf-Gladrow, *Lattice-Gas Cellular Automata and Lattice Boltzmann Models* (Springer-Verlag, Heidelberg, 2000).
24. A. N. Brooks and T. J. R. Hughes, Streamline upwind/Petrov-Galerkin formulation for convection dominated flows with particular emphasis on the incompressible Navier Stokes equation, *Comput. Method. Appl. Mech. Eng.* **32**, 199 (1982).
25. D. Noble, S. Chen, J. Georgiadis, and R. Buckius, A consistent hydrodynamic boundary condition for the lattice Boltzmann method, *Phys. Fluids* **7**(1), 203 (1995).
26. T. Inamuro, M. Yoshino, and F. Ogino, A non-slip boundary condition for lattice Boltzmann simulations, *Phys. Fluids* **7**(12), 2928 (1995).
27. R. Maier, R. Bernard, and D. Grunau, Boundary conditions for the lattice Boltzmann method, *Phys. Fluids* **8**(7), 1788 (1996).
28. Q. Zou and X. He, On pressure and velocity boundary conditions for the lattice Boltzmann BGK model, *Phys. Fluids* **9**(6), 1591 (1997).
29. S. Hou, Q. Zou, S. Chen, G. Dollen, and A. C. Cogley, Simulation of cavity flow by the lattice Boltzmann method, *J. Comput. Phys.* **118**, 329 (1995).
30. S. Chen, D. Martínez, and R. Mei, On boundary conditions in lattice Boltzmann methods, *Phys. Fluids* **8**(9), 2527 (1996).
31. T. C. Papanastasiou, N. Malamataris, and K. Ellwood, A new out flow boundary condition, *Int. J. Numer. Methods Fluids* **14**, 587 (1992).
32. R. L. Sani and P. M. Gresho, Résumé and remarks on the open boundary condition minisymposium, *Int. J. Numer. Methods Fluids* **18**, 983 (1994).
33. D. F. Griffiths, The "no boundary condition" outflow boundary condition, *Int. J. Numer. Methods Fluids* **24**, 393 (1997).
34. M. Renardy, Imposing "no" boundary condition at outflow: Why does it work? *Int. J. Numer. Methods Fluids* **24**, 413 (1997).

35. G. Comini, M. Manzan, and C. Nonino, Analysis of finite element schemes for convection-type problems, *Int. J. Numer. Methods Fluids* **20**, 443 (1995).
36. J. H. Ferziger and M. Perić, *Computational Methods for Fluid Dynamics* (Springer-Verlag, New York, 1999).
37. U. Ghia, K. N. Ghia, and C. T. Shin, High-Re solutions for incompressible flow using the Navier-Stokes equations and a multigrid method, *J. Comput. Phys.* **48**, 387 (1982).
38. C.-L. Lin and Y. Lai, Lattice Boltzmann method on composite grids, *Phys. Rev. E.* **62**(2), 2219 (2000).
39. J. D. Tritton, Experiments on the flow past a circular cylinder at low Reynolds numbers, *J. Fluid Mech.* **6**, 547 (1959).
40. S. C. R. Dennis and G. Z. Chang, Numerical solutions for steady flow past a circular cylinder at Reynolds number up to 100, *J. Fluid Mech.* **42**, 471 (1970).
41. F. Nieuwstadt and H. B. Keller, Viscous flow past circular cylinders, *Comput. Fluids* **1**, 59 (1973).
42. B. Fornberg, A numerical study of steady viscous flow past a circular cylinder, *J. Fluid Mech.* **98**, 819 (1980).